machines

MDPI

Article

Analytical Modeling and Analysis of High-Torque-Density Three-Segment Halbach Array PM Machine by Considering Leakage Flux

Jinlin Huang [1,2,*], Qingfeng Sun [1] and Chen Wang [3,4]

1 Electrical Engineering College, Anhui Technical College of Mechanical and Electrical Engineering, Wuhu 241002, China; 0125000356@ahcme.edu.cn
2 Key Laboratory of Electric Drive and Control of Anhui Province, Wuhu 241000, China
3 School of Electrical Engineering, Anhui Polytechnic University, Wuhu 241000, China; wch1071@ahpu.edu.cn
4 Wuhu Overseas Students' Entrepreneurship Park, Wuhu 241005, China
* Correspondence: 0125000562@ahcme.edu.cn

Abstract

Conventional finite element method (FEM) has a complex model and a long optimization time for Halbach array PM machines. This paper proposes a hybrid analytical method that combines the subdomain method (SM) and the magnetic circuit method (MEC) for analyzing a high-torque-density, three-segment Halbach array rotor permanent magnet (PM) machine, accounting for Halbach array magnetization and end leakage flux. Firstly, to address the challenge posed by complex PM shapes in the Halbach array PM machine, a novel subdivision equivalence method is conducted. Then, the magnetic equivalent circuit (MEC) of the stator and rotor is established, and the axial leakage flux and nonlinearity of the iron core are taken into account. In addition, electromagnetic performance, such as air gap flux density, cogging torque, electromagnetic torque, and back electromotive force (back-EMF), is obtained based on the proposed hybrid analytical model. The analytical results are verified by using the finite element method (FEM), and the results show that the error is less than 2%. Finally, a 15 kW prototype PM machine with a Halbach array PM rotor is manufactured and tested, and the results validate the accuracy and efficiency of the analytical method.

Keywords: analytical modeling; Halbach array PM; leakage flux; permanent magnet machine; subdomain model

Academic Editor: Payam Shams Ghahfarokhi

Received: 29 April 2026
Revised: 3 June 2026
Accepted: 5 June 2026
Published: 12 June 2026

1. Introduction

In recent years, permanent magnet (PM) machines have been widely adopted in various fields with the rapid electrification of transportation systems, such as electric vehicles (EVs), aerospace electric propulsion, and hybrid power systems, due to their high-power density, torque density, and efficiency [1–3].

Generally, the PM machines can be classified into surface-mounted PM (SPM) machines and interior PM (IPM) machines according to the position of the PMs. Concentrated winding SPM machines have a simpler rotor structure and higher torque density compared with IPM machines. As a special SPM machine, the Halbach array PM rotor can provide higher and sinusoidal air gap flux density to obtain higher power density, lower rotor weight, and excellent dynamic performances, and it has been studied in some of the literature [4–6]. To improve the efficiency, a Halbach array considering the third harmonic air gap flux density is proposed. The electromagnetic performances of the proposed Halbach array are compared with the PM machine with a conventional Halbach array [7]. In [8], a 270 kW dynamo motor is designed with a Halbach array using samarium–cobalt PMs, and the results show that the Halbach array motor is superior to a surface-mounted PM motor in torque performance. The PM widths and magnetization angles are optimized to obtain maximum torque for the Halbach PM machines in [9]. It is noted that the appropriate PM thickness, split ratio, and segment number can improve the torque density for Halbach PM machines. However, it is difficult to build the finite element (FE) model compared with other PM machines due to the special magnetization method for Halbach array PM machines, which leads to a long optimization cycle. The PM losses reduction method is investigated for the Halbach array PM to improve the efficiency [10]. Halbach array consequent-pole PM machine is proposed, and the torque quantification analysis of the main-order and modulated magnetic field harmonics is identified [11].

Accurately and quickly calculating the air gap magnetic field is the theoretical basis of PM machine design, optimization, and analysis. Compared with the finite element method (FEM), the subdomain method (SM) has obvious advantages, such as faster calculating speed, clearer physical mechanism, being highly instructive, and so on. The SM model for different PM machines has been presented in [12–14], including surface PM machine, surface-inset PM machine, and Halbach PM machine. However, the accuracy of the linear SM model is low because the effect of saturation is not taken into account. To solve the saturation problem, a nonlinear subdomain and magnetic circuit hybrid model for surface-mounted PM machines has been proposed in [15]. In [16,17], the winding function combined with MEC is proposed to obtain the air gap flux density under on-load conditions to reduce the error of the analytical model. An analytical method is proposed for calculating PM machine magnetic fields to consider the saturation effect by using the variable remanence method [16]. In [18,19], the magnetic saturation and eddy currents are considered by utilizing the MEC to obtain the solution for the nonlinear magnetic circuit. However, this method does not take into account the influence of the end leakage magnetic field. The spoke-type PM machines with trapezoidal and rectangular magnets are analyzed, and the PM is equivalent to two segments when considering the leakage magnetic field. Nevertheless, the proposed method is only appropriate for the spoke-type PM machines.

Although various PM machines with Halbach array PM and analytical method have been proposed and studied in previous investigations, the analytical method of the PM machine with Halbach array PM considering end leakage flux and PM magnetization has not been studied. Therefore, this article mainly focuses on presenting an analytical method to calculate the Halbach PM machine magnetic field considering Halbach PM magnetization, saturation, and axial end leakage. The main contributions can be summarized as follows:

(1) The production error of the analytical model is studied for a PM machine with a Halbach array PM under high torque density, and the SM modeling is proposed by considering the magnetization direction of the PM.

(2) The hybrid analytical model combining the SM and MEC is proposed to predict electromagnetic performance by considering the iron core saturation and end leakage effect, which improves the precision of the conventional method.

The rest of this paper is organized as follows: In Section 2, the configuration of the Halbach PM machine is introduced, and the key parameters are listed. Then, the analytical model is proposed to predict electromagnetic performance in Section 3. In Section 4, the air gap flux density, back-EMF, and electromagnetic torque under different conditions are calculated using the proposed analytical model, and the results are compared with the FEM model. Finally, a 15 kW prototype is manufactured and tested to validate the proposed analytical model in Section 6.

https://doi.org/10.3390/machines14060683

2. Topology of Halbach PM Machine

Figure 1 shows the configuration of a PM machine with Halbach array PM rotor, and the main parameters are listed in Table 1. It can be seen that the Halbach array PM is divided into three segments. In addition, the stator winding is fractional slot concentrated winding, which can reduce winding end length and improve efficiency. In addition, the configuration of Halbach array PM is shown in Figure 1c, and the θ_m is the angle between the magnetization direction of the associate pole and the main pole, and the θ_m is 90° in this paper to simplify the manufacturing process of the prototype.

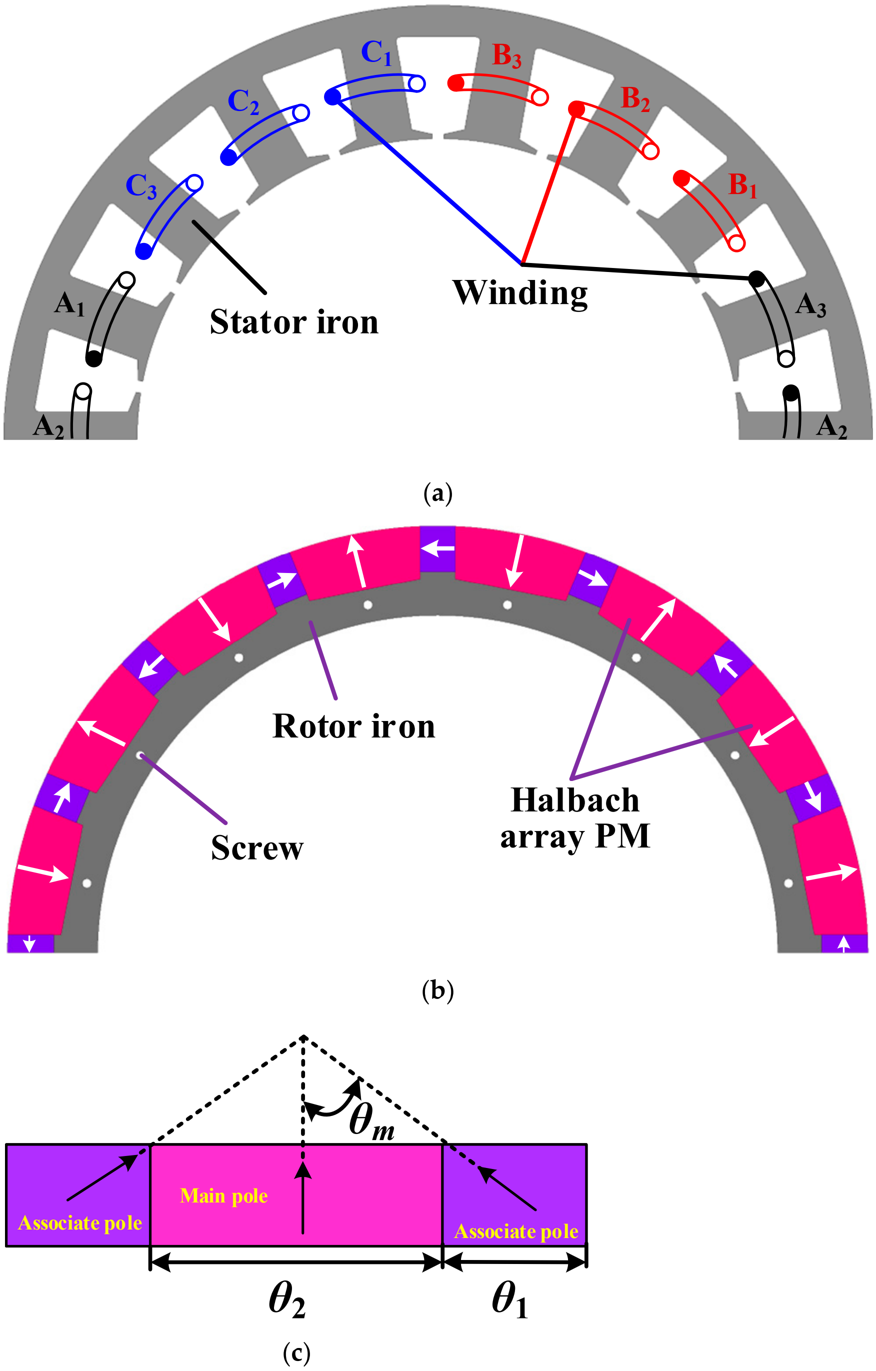

Figure 1. Configuration of Halbach array PM machine. (**a**) Stator; (**b**) rotor, (**c**) Halbach PM array.

Table 1. Main parameters of the Halbach array PM machine.

Parameters	Value	Parameters	Value
Stator outer diameter	290 mm	Stator inner diameter	201 mm
Rotor outer diameter	196 mm	Axial length	40 mm
Pole pairs	8	Stator slots	18
Air gap length	2.5 mm	PM outer diameter	196 mm
Rated current	40 A	Rated power	15 kW

To obtain the analytical model of the PM machine with Halbach array PM rotor, the opening position of the stator *i*-th slot can be expressed as

$$\alpha_i = \frac{2\pi i}{Q_s} - \frac{\pi}{Q_s},\ 1 \le i \le Q_s \tag{1}$$

where Q_s is the number of stator slot.

Then, the *k*-th main N-pole position of the Halbach PM rotor can be expressed as

$$\gamma_k = \frac{2\pi(k-1)}{p} + \delta,\ 1 \le k \le \mathrm{p} \tag{2}$$

where p is the number of pole pairs, and δ is the angle between the first N-pole PM and the position of the first stator slot opening.

3. Solution of the Subdomain with Field Source Excitation

In order to simplify the analytical model, the following basic assumptions are carried out: (1) The electrical conductivities for each of the parts are neglected. (2) The magnetic permeability of the core material is infinitely large. (3) PM material has the property of linear demagnetization. (4) The Halbach array PM is equivalent to the arc-shaped PM. (5) The current density has only a component along the z-axis direction.

The conventional SM of the PM machines is proposed in some of the literature [12,13], and an improved 2-D subdomain model accounting for Halbach array PM rotor is designed, as shown in Figure 2. In the proposed model, the PM machine is divided into five layers based on differences in excitation source and magnetic medium, which consist of the Halbach array PM layer (I), air gap layer (II), stator tooth tip (III), stator tooth layer (IV), and armature winding layer (V). Here, R_1, R_m, R_s, R_c and R_y are the rotor yoke diameter, PM outer diameter, stator inner diameter, stator slot inner diameter, and stator slot bottom diameter, respectively. In addition, θ_t, θ_s, θ_{tw} and θ_{sw} are the stator tooth tip width, stator slot opening width, stator tooth width, and stator slot width, respectively.

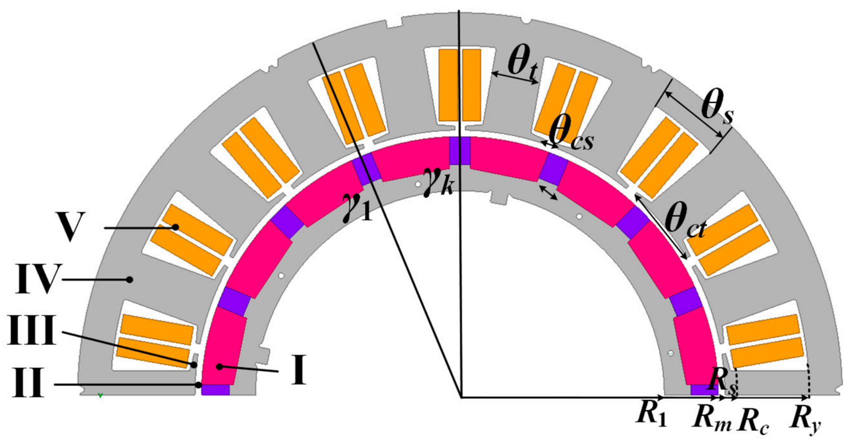

Figure 2. Analytical model and parameter illustration.

3.1. Stator Slot Subdomain

Due to the magnetic intensity vector not existing in the stator slots, the armature current serves only as field-source excitation, and the internal vector magnetic potential distribution satisfies the Poisson equation, which can be expressed as follows [15]

$$\frac{\partial^2 A_{5j}}{\partial r^2} + \frac{1}{r}\frac{\partial A_{5j}}{\partial r} + \frac{1}{r^2}\frac{\partial^2 A_{5j}}{\partial \theta^2} = -\mu_{copper} J_{jc} \quad (3)$$

where μ_{cooper} is the copper permeability, J_{jc} is the current density, A_{5j} is the stator slot vector magnetic potential, r is the radial coordinate, and θ is the tangential coordinate.

Then, the distribution of current density under the j-th stator slot is followed by [17]

$$J_{jc} = \begin{cases} J_{j1} & \theta_{sj} - \gamma_{sl} \le \theta \le \theta_{sj} \\ J_{j2} & \theta_{sj} \le \theta \le \theta_{sj} + \gamma_{sl} \end{cases} \quad (4)$$

The winding current density is periodically distributed, which can be expressed as a Fourier series

$$J_{jc} = J_{j0} + \sum_{n=1}^{\infty} J_{jn} \cdot \cos\left(\frac{n\pi}{\gamma_{sl}}\left(\theta - \theta_{sj} + \frac{1}{2}\gamma_{sl}\right)\right) \quad (5)$$

$$J_{j0} = \frac{(J_{j1} + J_{j2})}{2} \quad (6)$$

$$J_{jn} = \frac{2}{n\pi}(J_{j1} + J_{j2}\cos n\pi)\sin\frac{n\pi}{2} \quad (7)$$

Therefore, the vector magnetic potential distribution function can be obtained

$$\begin{aligned} A_{5j} &= A_{5j}^{com} + A_{5j}^{par} \\ &= a_{5j0} + \frac{1}{4}\mu_{copper} J_{j0}\left(2{R_{sl}}^2 \ln r - r^2\right) + \sum_{q=1}^{\infty} b_{5jn}\left(\left(\frac{r \cdot R_t}{{R_y}^2}\right)^{\frac{n\pi}{\theta_s}} + \left(\frac{r}{R_t}\right)^{-\frac{n\pi}{\theta_s}}\right) \cdot \cos\left(\frac{n\pi}{\delta}\left(\theta - \theta_{sj} + \frac{\delta}{2}\right)\right) \\ &+ \sum_{n=1}^{\infty} \frac{\mu_{copper} J_{jn}}{\left(\frac{n\pi}{\theta_s}\right)^2 - 4}\left(r^2 - \frac{2\theta_s}{n\pi}{R_y}^2\left(\frac{r}{R_y}\right)^{\frac{n\pi}{\theta_s}}\right) \cdot \cos\left(\frac{n\pi}{\theta_s}\left(\theta - \theta_{sj} + \frac{R_y}{2}\right)\right) \end{aligned} \quad (8)$$

a_{4j0} is the coefficient of stator slot vector magnetic potential, which can be obtained by non-homogeneous equations.

3.2. PM Subdomain

In addition, the magnetization intensity of three-segment Halbach array PM can be decomposed into radial and tangential components in the two-dimensional polar coordinate system. Therefore, the radial magnetization intensity M_r(θ) and tangential magnetization intensity M_θ(θ) can be obtained according to the magnetization direction of each PM.

$$M_r(\theta) = \begin{cases} \frac{B_r}{\mu_0}\cos\theta_m, \theta \in [\gamma_k - \theta_1 - \frac{\theta_2}{2}, \gamma_k - \frac{\theta_2}{2}] \\ \frac{B_r}{\mu_0}, \theta \in [\gamma_k - \frac{\theta_2}{2}, \gamma_k + \frac{\theta_2}{2}] \\ \frac{B_r}{\mu_0}\cos\theta_m, \theta \in [\gamma_k + \frac{\theta_2}{2}, \gamma_k + \theta_1 + \frac{\theta_2}{2}] \\ -\frac{B_r}{\mu_0}\cos\theta_m, \theta \in [\gamma_k + \theta_1 + \frac{\theta_2}{2}, \gamma_k + 2\theta_1 + \frac{\theta_2}{2}] \\ -\frac{B_r}{\mu_0}, \theta \in [\gamma_k + 2\theta_1 + \frac{\theta_2}{2}, \gamma_k + 2\theta_1 + \frac{3\theta_2}{2}] \\ -\frac{B_r}{\mu_0}\cos\theta_m, \theta \in [\gamma_k + 2\theta_1 + \frac{\theta_2}{2}, \gamma_k + 3\theta_1 + \frac{3\theta_2}{2}] \end{cases} \quad (9)$$

$$M_\theta(\theta) = \begin{cases} \frac{B_r}{\mu_0}\sin\theta_m, \theta \in [\gamma_k - \theta_1 - \frac{\theta_2}{2}, \gamma_k - \frac{\theta_2}{2}] \\ 0, \theta \in [\gamma_k - \frac{\theta_2}{2}, \gamma_k + \frac{\theta_2}{2}] \\ -\frac{B_r}{\mu_0}\sin\theta_m, \theta \in [\gamma_k + \frac{\theta_2}{2}, \gamma_k + \theta_1 + \frac{\theta_2}{2}] \\ -\frac{B_r}{\mu_0}\sin\theta_m, \theta \in [\gamma_k + \theta_1 + \frac{\theta_2}{2}, \gamma_k + 2\theta_1 + \frac{\theta_2}{2}] \\ 0, \theta \in [\gamma_k + 2\theta_1 + \frac{\theta_2}{2}, \gamma_k + 2\theta_1 + \frac{3\theta_2}{2}] \\ -\frac{B_r}{\mu_0}\sin\theta_m, \theta \in [\gamma_k + 2\theta_1 + \frac{\theta_2}{2}, \gamma_k + 3\theta_1 + \frac{3\theta_2}{2}] \end{cases} \quad (10)$$

where B_r is the residual flux density, and μ_0 is the vacuum permeability.

Similarly, the magnetization intensity can also be expressed as a complex form of Fourier series based on Fourier transformation principle.

$$M_r(\theta) = \sum_{n=-N}^{N} \hat{M}_{r,n} e^{-jn\theta} \quad (11)$$

$$M_\theta(\theta) = \sum_{n=-N}^{N} \hat{M}_{\theta,n} e^{-jn\theta} \quad (12)$$

3.3. Air Gap Subdomain

According to the differential equation, the stator slot opening area (III) solution can be followed by

$$A_{3j} = a_{3j0} + b_{3j0}\ln(r) + \sum_{n=1}^{\infty}\left[c_{3jn}\left(\frac{r}{R_t}\right)^{\frac{n\pi}{\gamma}} + d_{3jn}\left(\frac{r}{R_s}\right)^{-\frac{n\pi}{\gamma}}\right]\cos\left(\frac{n\pi}{\gamma}\left(\theta - \theta_{sj} + \frac{\gamma}{2}\right)\right) \quad (13)$$

a_{3j0} and b_{3j0} are the coefficient of air gap subdomain vector magnetic potential, which can be obtained through non-homogeneous equations.

The subdomain without external source excitation is mainly the air gap domain (II), which is required solving the homogeneous Laplace equation. The air gap equation solution can be expressed as follows

$$A_{2j} = \sum_{n=1}^{\infty}\left[a_{2n}\left(\frac{r}{R_s}\right)^{n} + b_{2n}\left(\frac{r}{R_r}\right)^{-n}\right]\cos(n\theta) + \sum_{n=1}^{\infty}\left[c_{2n}\left(\frac{r}{R_s}\right)^{n} + d_{2n}\left(\frac{r}{R_r}\right)^{-n}\right]\sin(n\theta) \quad (14)$$

a_{2j0} is the coefficient of air gap subdomain vector magnetic potential, which can be obtained through non-homogeneous equations. R_s and R_r are the stator inner radius and rotor outer radius, respectively. a_{2n} and b_{2n} are the integration coefficient in this paper.

It can be noted that Equations (1)–(14) are the general form of the equation. Based on this, when harmonic orders are incorporated into the vector potential distribution function is considered the, the calculation accuracy is achieved. However, the number of unknown coefficients existed in the expression, which significantly increased the difficulty of the calculation. Therefore, the maximum harmonic order is considered when calculating the vector potential expression, achieving a balance between the calculation amount and the calculation accuracy.

3.4. Analysis of Magnetic Leakage Characteristic

Due to the fundamental assumption of magnetic permeability in the core region within the SM, the accuracy is reduced, especially for high torque density, high air gap magnetic flux, and high core saturation. Meanwhile, the magnetic resistance of the main magnetic path is significantly increased under high-load conditions, which leads to an increase in the leakage magnetic flux, and the torque output capacity of the PM machine is also decreased.

Figure 3 shows the distribution of leakage flux under high-load conditions. It can be seen that the leakage flux consists of rotor air gap leakage flux and rotor end leakage flux. According to the MEC, the rotor axial leakage permeance and stator tooth axial leakage permeance can be expressed as follows [20,21]

$$P_{sen} = 0.264\mu_0 \times H_{sn} \tag{15}$$

$$P_{ten} = \frac{H_{sn}}{\pi} \cdot \frac{\mu_0 \cdot \ln(1 + \frac{\pi(R_{ao.n}+R_{ai.n})}{(0.5\times Q_s)} - W_{sn})}{W_{sn}} \tag{16}$$

where R_{ao_n} and R_{ai_n} denote the outer and inner radius of the n-th air region, respectively.

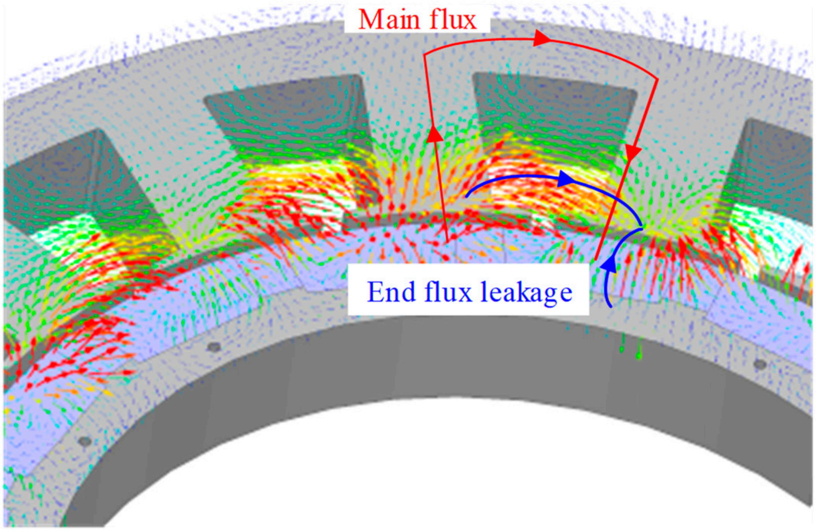

(**a**)

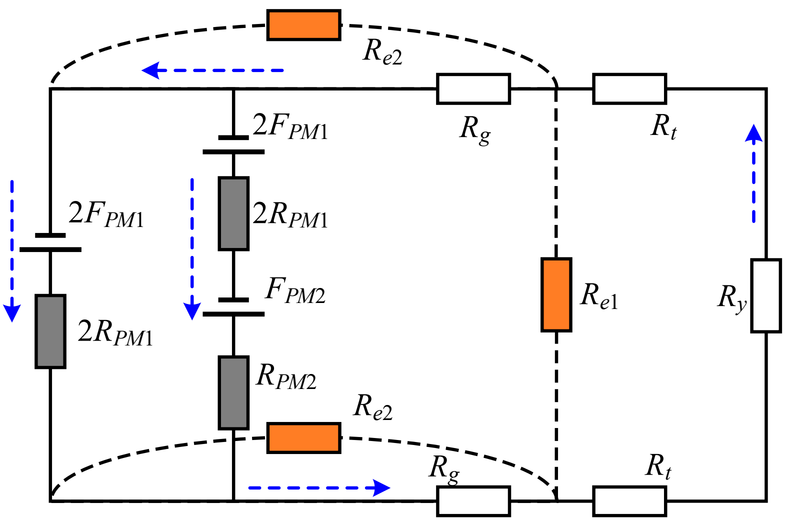

(**b**)

Figure 3. Distribution of leakage flux. (**a**) FEM results; (**b**) leakage magnetic equivalent circuit.

Therefore, the main magnetic flux under non-ideal conditions can be obtained as

$$\Phi_{nonideal} = \frac{F_{pm}}{R_{pm} + R_{al} \parallel R_{bl} \parallel \left(2R_{rp} + R_{gl} \parallel R_1\right)} \cdot \frac{R_{al} \parallel R_{bl}}{R_{al} \parallel R_{bl} + \left(2R_r + R_{gl} \parallel R_1\right)} \cdot \frac{R_{gl}}{R_{gl} + R_1} \tag{17}$$

To consider the influence of stator tooth magnetic resistance on air gap flux density, the stator tooth magnetic resistance is integrated with the air gap magnetic resistance proposed in this paper, which can be expressed as

$$R_{tj} = R_{tj1} + R_{tj2} + \left(R_{ttj1} \parallel R_{ttj2} \parallel R_{ttj3}\right) \tag{18}$$

$$R_{agj} = \frac{1}{\mu_{air}} \frac{\delta}{W_t \cdot L_{ef}} \tag{19}$$

where j = 1, 2, 3, 4, . . ., 18. The equivalent air gap magnetic permeability for the analytical model can be expressed as follows

$$\mu_{eqj} = \frac{\delta}{W_t \cdot L_{ef}} \frac{1}{R_{agj} + R_{tj}} \tag{20}$$

where W_t denotes stator tooth width.

To achieve data coupling between the MEC and the SM, the magnetic flux flowing into the stator inner surface can be obtained by integrating the air gap flux density along the inner circle of the stator based on the SM, which is then regarded as another excitation source for the stator magnetic circuit. This can be expressed as

$$\Phi_{j1} = R_s L_{ef} \int\limits_{\theta_{sj}-(\alpha_{st}+\alpha_{so})/2}^{\theta_{sj}-\alpha_{st}/2} B_r(R_s, \theta) d\theta \tag{21}$$

$$\Phi_{j2} = R_s L_{ef} \int\limits_{\theta_{sj}-\alpha_{st}/2}^{\theta_{sj}+\alpha_{st}/2} B_r(R_s, \theta) d\theta \tag{22}$$

$$\Phi_{j3} = R_s L_{ef} \int\limits_{\theta_{sj}+\alpha_{st}/2}^{\theta_{sj}+(\alpha_{st}+\alpha_{so})/2} B_r(R_s, \theta) d\theta \tag{23}$$

Then, the nodal voltage matrix equation of the Halbach array PM machine is obtained based on Kirchhoff's laws [22–24]:

$$\mathbf{G}\,\mathbf{U} = \mathbf{\Phi} \tag{24}$$

where G is the magnetic conductance matrix.

3.5. Ai -Gap Flux Density and Torque

Finally, the electromagnetic performance of the Halbach array PM machine is predicted based on the magnetic field solution, including air gap flux density, cogging torque, back-EMF, and electromagnetic torque.

Based on the expression of vector potential, the no-load air gap flux density can be expressed as

$$B_r = \frac{1}{r} \frac{\partial A}{\partial \theta} \tag{25}$$

$$B_\theta = -\frac{\partial A}{\partial \theta} \tag{26}$$

For double-layer stator windings, the phase A back-EMF can be expressed as follows

$$E_A = -\frac{d\Psi_A}{dt} = \frac{2N_c L_{ef}}{S_s} \left(\int_{R_t}^{R_{sl}} \int_{\theta_{sj}-\delta/2}^{\theta sj} A_{4j} r dr d\theta - \int_{R_t}^{R_{sl}} \int_{\theta_{sj-1}}^{\theta_{sj-1}+\delta/2} A_{4j-1} r dr d\theta \right) \tag{27}$$

The no-load cogging torque can be obtained based on the Maxwell stress tensor method, and it can be expressed as

$$T_{ct} = \frac{L_{ef} r^2}{\mu_{air}} \int_0^{2\pi} B_r B_\theta d\theta = \frac{\pi L_{ef} r^2}{\mu_{air}} \sum_{k=1}^{K} B_{rck} B_{\theta ck} + B_{rsk} B_{\theta sk} \tag{28}$$

On the other hand, the on-load electromagnetic torque can be calculated when the stator winding has a current source, and it can be expressed as follows:

$$T_e = \frac{E_A I_A + E_B I_B + E_C I_C}{\Omega} \tag{29}$$

4. Comparison and Analysis of Electromagnetic Performance

4.1. No-Load Characteristics

A 2-D FE model is established to verify the analytical modeling since the stator core saturation level is low. Figure 4 shows the distribution of flux density and line of the Halbach array PM machine based on the FE model. It can be seen that the stator core maximum flux density is about 2.1 T, and it is lower than the core saturation magnetic density.

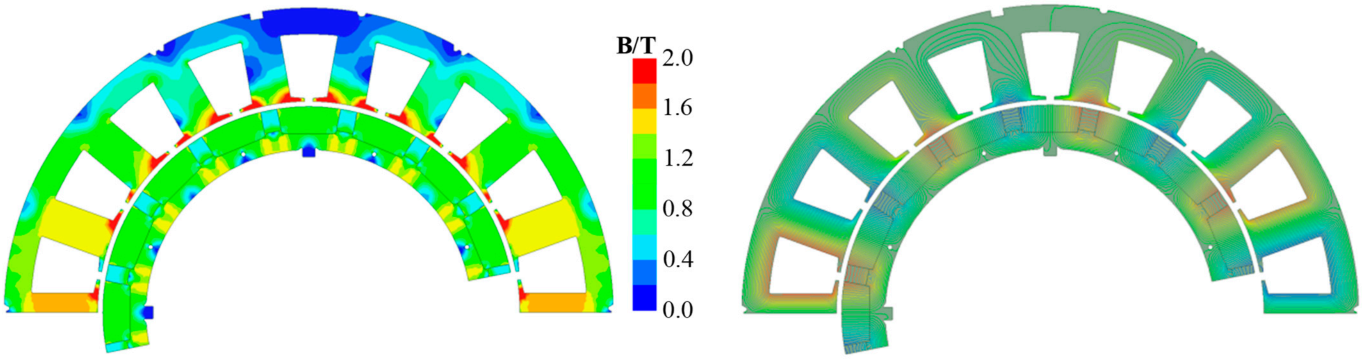

(**a**) (**b**)

Figure 4. Distribution of flux density and line of the Halbach array PM machine. (**a**) Flux density distribution; (**b**) magnetic line distribution.

In addition, the radial and tangential air gap flux densities are calculated through FEM and the proposed analytical model, as shown in Figure 5. It can be observed that the analytical model waveform is greatly consistent with the FEM waveform. The maximum radial air gap flux density is about 1.15 T based on the FEM model, which is lower than the prediction of the analytical model of about 1.13 T. The tiny differences between the two waveforms are caused by the saturated iron material and the higher-order harmonics. As can be seen from Figure 5a, there are noticeable dips in the amplitude of the air gap magnetic flux density at some angular positions. This is mainly due to the fact that the tangential PMs in the Halbach Array are directly facing the stator slot. Figure 5b shows the tangential air gap flux density. It can be seen that it is not perfectly sinusoidal because the tangential flux density is the circumferential component of the magnetic field, which inherently has a smaller amplitude, is more sensitive to field distortion, and possesses a higher harmonic content. In addition, it can be observed that the tangential component of the flux density is relatively small compared with radial flux density.

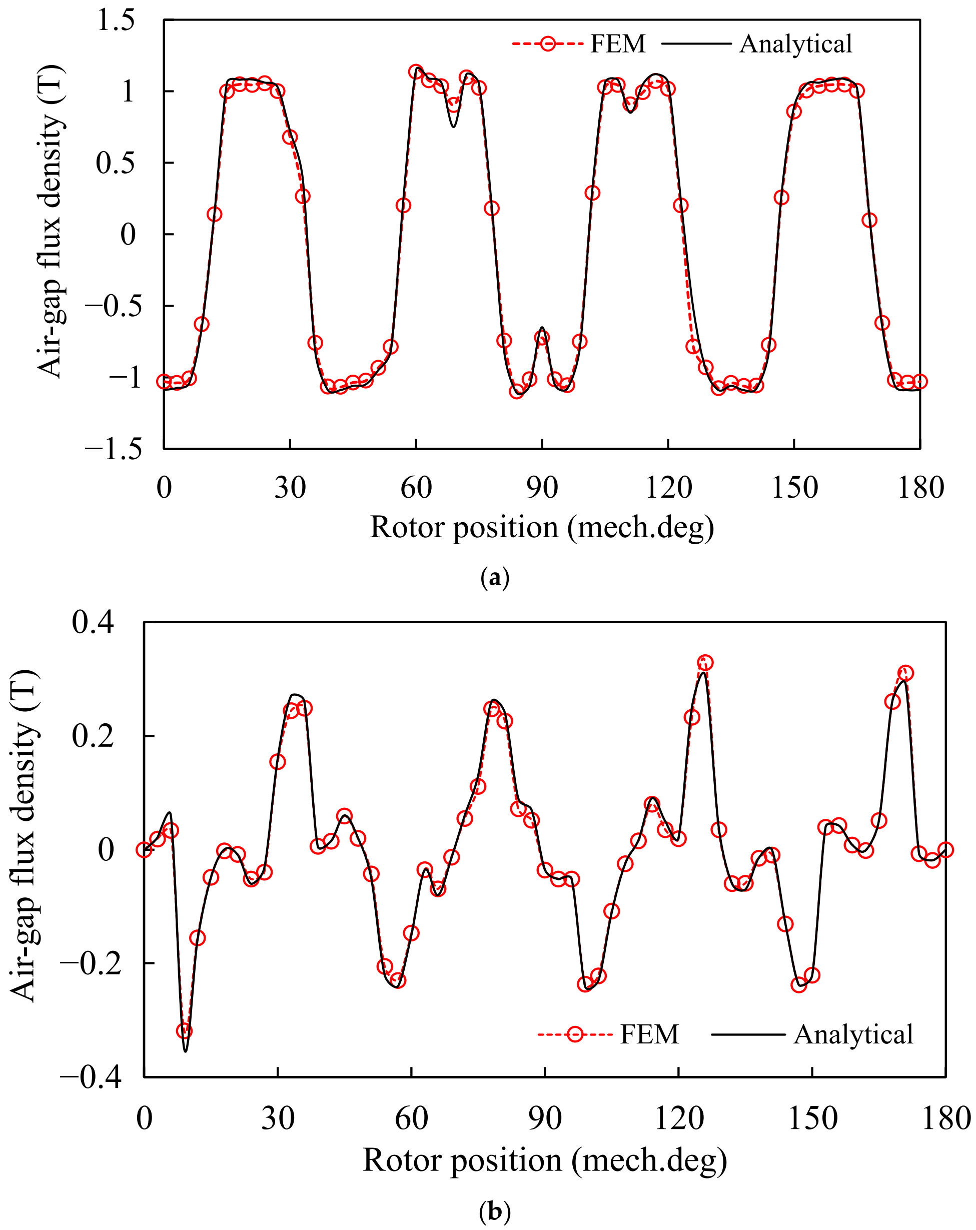

Figure 5. No-load air gap flux density. (**a**) Radial component; (**b**) circumferential component.

Figure 6 shows the comparison between no-load back-EMF and cogging torque waveforms. It can be seen that the waveforms of analytical results are in very good agreement with the FEM results. However, the amplitude of analytical cogging torque is lower than that obtained through the FEM, which is caused by the small error between the analytically and FEA-calculated air gap flux density. One source of error is mesh generation in the FE model, and another source of error stems from the need to integrate the radial and tangential magnetic flux densities along the circumference, which can accumulate errors in the cogging torque calculation based on the Maxwell stress tensor method used in this paper. From this, it can be seen that the accuracy of the proposed analytical model under no-load condition is very close to that of the FEM model.

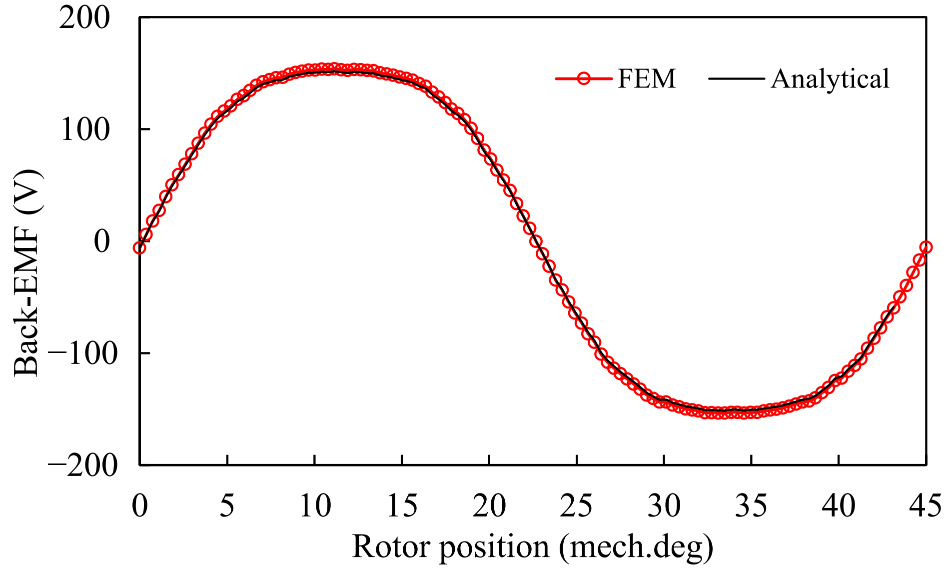

(**a**)

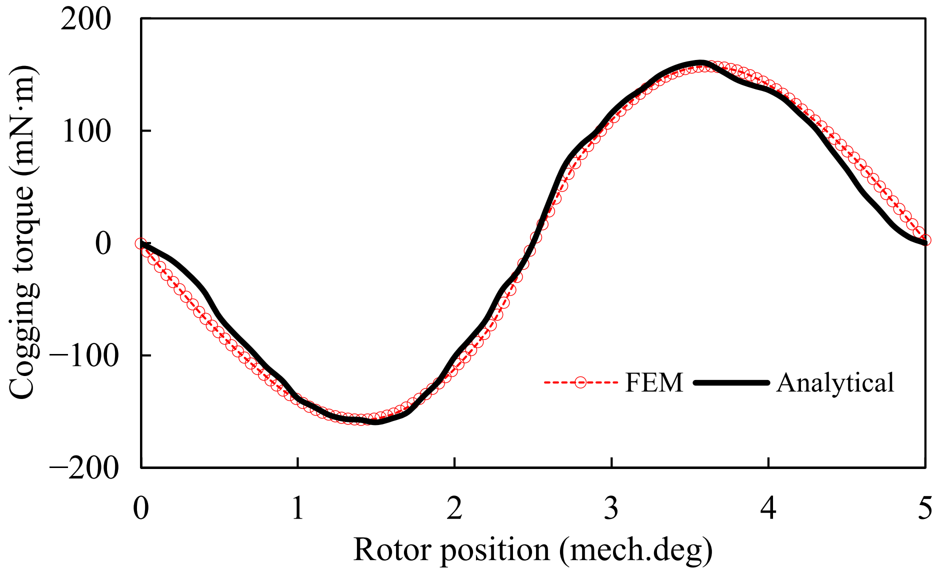

(**b**)

Figure 6. No-load back-EMF and cogging torque. (**a**) back-EMF; (**b**) cogging torque.

4.2. On-Load Characteristics

The electromagnetic torque under different phase currents is shown in Figure 7a. It can be seen that the output torque increases linearly with the increase in phase current. The maximum torque can achieve 353 N·m and 351 N·m based on 2-D FEM and analytical models without end leakage flux, but the maximum torque is only 262 N·m and 275 N·m. The error is about 25.7%, and the reason for this is that the end leakage flux is considered based on the 3-D FEM and the hybrid analytical model. The hybrid analytical model and 3-D FEM results are in very good agreement in this paper due to the fact that end leakage flux is considered. The slight error in the torque waveforms is generated due to the accumulation of errors in the calculated air gap flux density over time.

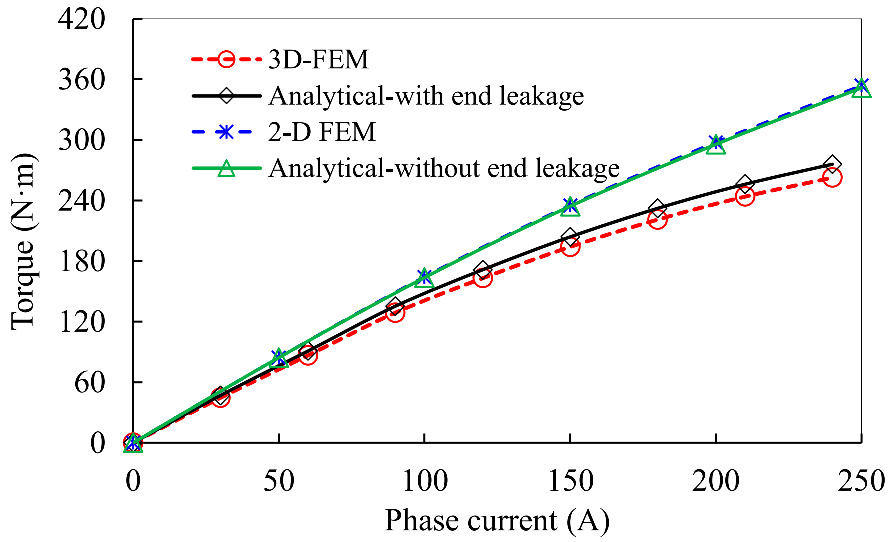

(**a**)

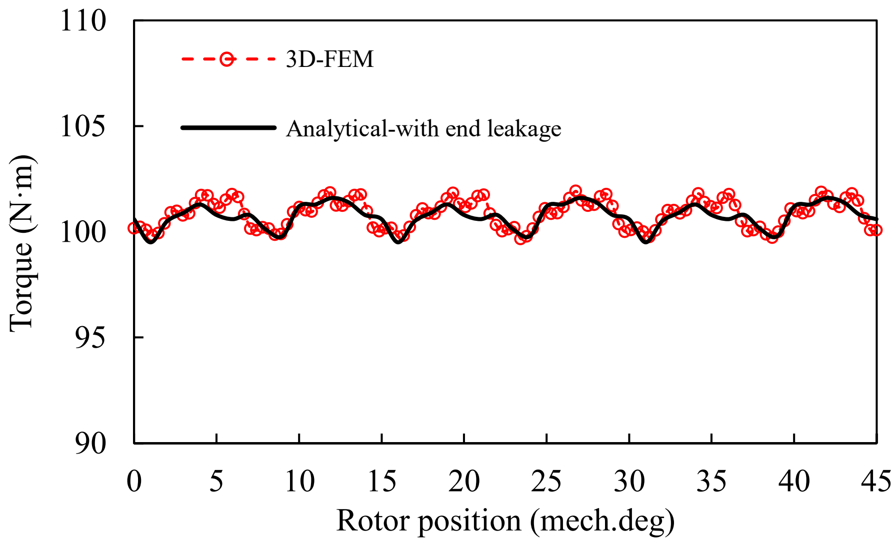

(**b**)

Figure 7. On-load torque characteristics. (**a**) Torque versus phase current; (**b**) torque waveform.

In addition, the average torque waveforms of the FEM and analytical model are shown in Figure 7b. It can be seen that the average torque is about 101 N·m and 100 N·m under rated current density, respectively. The error is lower than 2%, and the changing trend of the two results is highly consistent.

5. Experimental Verification

In order to verify the correction of analytical modeling results, a 15 kW PM machine with three-segment Halbach array PM rotor has been fabricated. Figure 8a,b show the prototype of stator and rotor assembly. The carbon fiber sleeve is employed to ensure the PM machine's secure operation. Then, to evaluate the performance of the prototype, the experimental platform is established, including the PM prototype, prime motor, oscilloscope, torque sensor, and so on, as shown in Figure 8c.

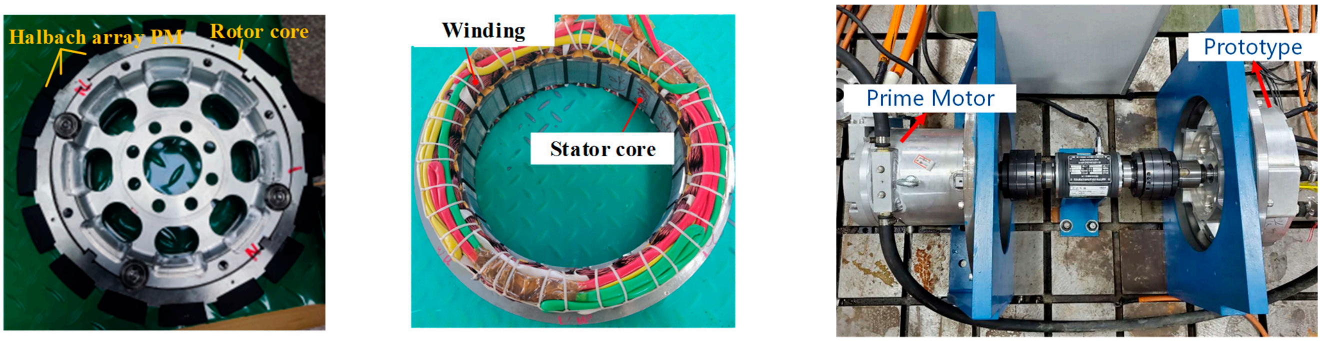

(**a**) (**b**) (**c**)

Figure 8. Prototype and experimental platform. (**a**) Rotor; (**b**) stator; (**c**) platform.

First, the no-load test is carried out, and the no-load back-EMF is measured under 2400 r/min, as shown in Figure 9. It can be seen that the no-load back-EMF is closely resembles a sinusoidal waveform. The effective value of tested back-EMF is about 213 V, which is in good agreement with the FEM and analytical modeling. However, a deviation remains between the amplitude of the tested back-EMF and analytical modeling, and the reason for this stems from the inherent errors arising from the assumption and the actual model.

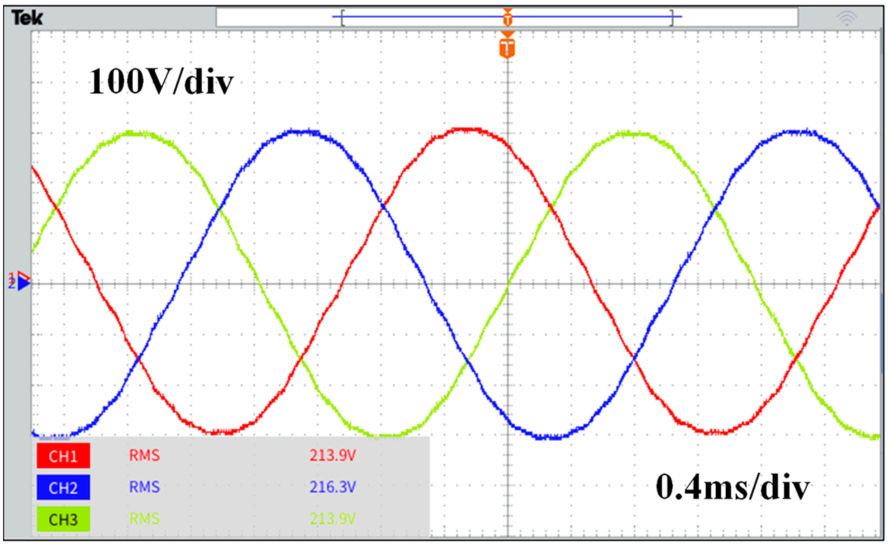

Figure 9. Measured line back-EMF under 2400 r/min.

In addition, the torque sensor is connected between the PM machine prototype and prime motor, and the electromagnetic torque versus phase current performance is shown in Figure 10. It can be seen that the tested results and the hybrid analytical model are in excellent agreement due to the fact that iron core saturation and axial leakage flux are considered. The phase current waveform is shown in Figure 11. The comparison between the analytical and experimental results indicates that the proposed analytical modeling method has great accuracy when used for predicting the electromagnetic performance of the high-torque-density Halbach array PM machine.

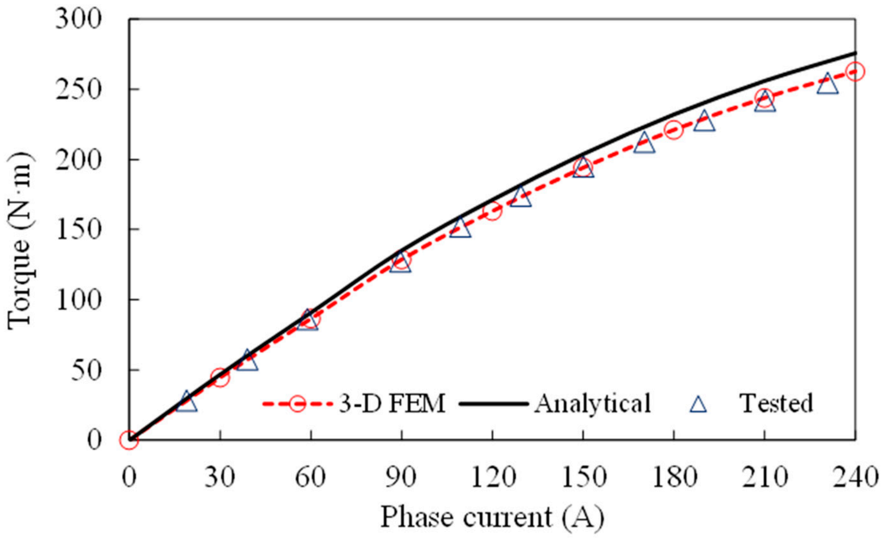

Figure 10. Measured torque versus phase current under 2400 r/min.

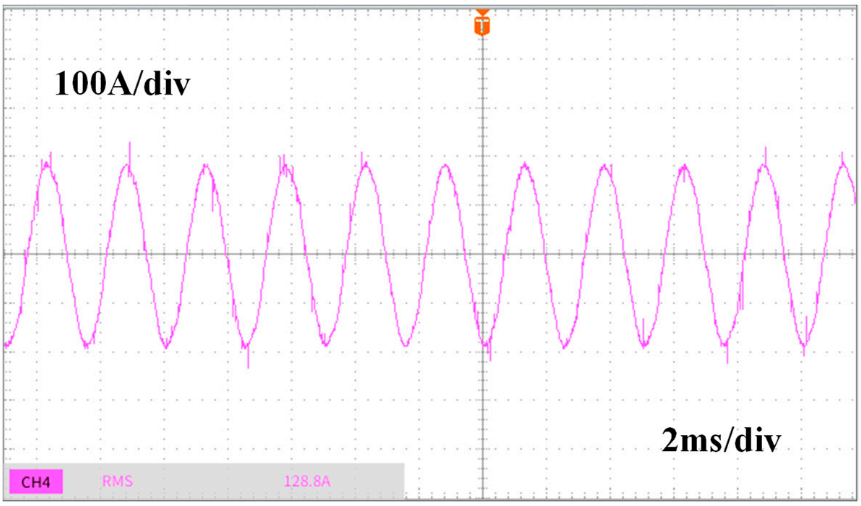

Figure 11. Measured phase current waveform under 3000 r/min.

6. Conclusions

This paper presents a hybrid analytical model for predicting the field distribution and electromagnetic characteristics of the high-torque-density Halbach array PM machine by considering end leakage flux and special rotor structure. The end leakage flux MEC model is built considering the stator iron core saturation and end axial end leakage flux, which reduces calculation error for traditional analytical model. Successful validation within 5% error was performed against 3-D FEM and experimental results from prototype Halbach array PM machine. The models derived for no-load air gap flux density, back-EMF, cogging torque, and average torque, are the most useful for preliminary design. According to a comprehensive comparison study, the proposed hybrid analytical model demonstrates great speed superiority without sacrificing accuracy. In addition, although the topic of this paper is focused on three-segment Halbach array PM machine, for SPM machines with regular-shaped PM, the new proposed AM is still more efficient than traditional analytical model, especially for high-torque and high-power-density PM machine.

Author Contributions: Conceptualization, J.H.; methodology, J.H.; formal analysis, Q.S.; investigation, J.H.; resources, J.H. and C.W.; writing—original draft preparation, J.H.; writing—review and editing, J.H. and C.W.; supervision, Q.S. All authors have read and agreed to the published version of the manuscript.

Funding: This work was supported by the Natural Science Research Project of Anhui Province of P. R. China (2024AH050219, 2023AH052697) and the Key Laboratory of Electric Drive and Control of Anhui Province, Anhui Polytechnic University (DQKJ202507).

Data Availability Statement: The original contributions presented in this study are included in the article. Further inquiries can be directed to the corresponding author.

Conflicts of Interest: The authors declare no conflicts of interest.

References

1. St-Jacques, B.B.; Shi, R.; Pillay, P. An enhanced PMSM cooling design for traction of an electric vehicle. *IEEE Trans. Transp. Electrif.* **2024**, *10*, 3845–3854. [CrossRef]
2. Brelje, B.J.; Martins, J.R.R.A. Electric, hybrid, and turboelectric fixed-wing aircraft: A review of concepts, models, and design approaches. *Prog. Aerosp.* **2019**, *104*, 1–19. [CrossRef]
3. Nishanth, F.; Bohach, G.; Nahin, M.M.; de Ven, J.V.; Severson, E.L. Development of an integrated electro-hydraulic machine to electrify off highway vehicles. *IEEE Trans. Ind. Appl.* **2022**, *58*, 6163–6174. [CrossRef]
4. Wei, L.; Nakamura, T. A Novel Dual-Stator Hybrid Excited Permanent Magnet Vernier Machine with Halbach-Array PMs. *IEEE Trans. Magn.* **2021**, *57*, 8101705. [CrossRef]
5. Shen, Y.; Lu, Q.; Li, Y. Design Criterion and Analysis of Hybrid-Excited Vernier Reluctance Linear Machine with Slot Halbach PM Arrays. *IEEE Trans. Ind. Electron.* **2023**, *70*, 5074–5084. [CrossRef]
6. Gao, Y.; Li, J.; Liu, Y.; Li, Z. Analysis of a Vernier Machine with Buried Halbach-Array Permanent Magnets. *IEEE Trans. Transp. Electrif.* **2025**, *11*, 4035–4046. [CrossRef]
7. Zhang, L.F.; Wang, K.; Sun, H.Y.; Zhu, S.S. Multiphase PM Machines with Halbach Array Considering Third Harmonic Flux Density. *IEEE Trans. Ind. Electron.* **2019**, *66*, 9184–9193. [CrossRef]
8. Koo, B.; Kim, J.; Nam, K. Halbach Array PM Machine Design for High Speed Dynamo Motor. *IEEE Trans. Magn.* **2021**, *57*, 8202105. [CrossRef]
9. Li, Y.; Zhu, Z.Q.; Xiang, D.; Brockway, S.; Manss, M.; Lea, J.; Ren, Y. Influence of Rotor Back-Iron on Optimal Halbach PM Machines. *IEEE Trans. Energy Convers.* **2025**, *41*, 1791–1804. [CrossRef]
10. Hebala, A.; Nuzzo, S.; Connor, P.H.; Giangrande, P.; Gerada, C.; Galea, M. PM Halbach Arrays in Motors: Loss Reduction and Performance Improvements. In Proceedings of the 23rd International Conference on Electrical Machines and Systems (ICEMS), Hamamatsu, Japan, 24–27 November 2020.
11. Li, Y.; Zhou, Q.; Ding, S.; Hang, J.; Li, W. Quantitative Evaluation of Torque Contributions of Multiple Working Harmonics on Halbach Array Consequent-Pole PM Machine. *IEEE ASME Trans. Mechatron.* **2024**, *29*, 4572–4581. [CrossRef]
12. Rahideh, A.; Mardaneh, M.; Korakianitis, T. Analytical 2-D calculations of torque, inductance, and back-EMF for brushless slotless machines with surface inset magnets. *IEEE Trans. Magn.* **2013**, *49*, 4873–4884. [CrossRef]
13. Ni, Y.; Chen, K.; Xiao, B.; Qian, W.; Wang, Q. Analytical modeling of PM electrical machines with eccentric surface-inset Halbach magnets. *IEEE Trans. Magn.* **2021**, *57*, 8104309. [CrossRef]
14. Boroujeni, S.T.; Naghneh, H.B. Analytical modelling and prototyping a slotless surface-inset PM machine. *IET Electr. Power Appl.* **2017**, *11*, 312–322. [CrossRef]
15. Wu, L.J.; Zhu, Z.Q.; Staton, D.; Popescu, M.; Hawkins, D. An improved subdomain model for predicting magnetic field of surface mounted permanent magnet machines accounting for tooth-tips. *IEEE Trans. Magn.* **2011**, *47*, 1693–1704. [CrossRef]
16. Hoang, K. Simplified analytical model for rapid evaluation of interior PM traction machines considering magnetic nonlinearity. *IEEE Open J. Ind. Electron. Soc.* **2020**, *1*, 340–354. [CrossRef]
17. Li, Q.; Fan, T.; Wen, X. Armature-reaction magnetic field analysis for interior permanent magnet motor based on winding function theory. *IEEE Trans. Magn.* **2013**, *49*, 1193–1201. [CrossRef]
18. Zhou, H.; Wang, X.; Zhao, W.; Xing, Z.; Li, X. Magnetic field calculation of the U-shaped interior permanent-magnet synchronous machine considering the parallel magnetization and bridge saturation. *IEEE Trans. Ind. Electron.* **2024**, *71*, 11817–11828. [CrossRef]
19. Mahmoud, H.; Bianchi, N.; Bacco, G.; Chiodetto, N. Nonlinear analytical computation of the magnetic field in reluctance synchronous machines. *IEEE Trans. Ind. Appl.* **2017**, *53*, 5373–5382. [CrossRef]
20. Jung, J.-W.; Park, H.-I.; Hong, J.-P.; Lee, B.-H. A novel approach for 2-D electromagnetic field analysis of surface mounted permanent magnet synchronous motor taking into account axial end leakage flux. *IEEE Trans. Magn.* **2017**, *53*, 8208104. [CrossRef]

21. Jung, J.-W.; Lim, M.-S.; Hong, J.-P.; Lee, B.-H. Characteristics analysis of SPMSM using 2-D finite-element analysis considering axial leakage flux. *IEEE Trans. Magn.* **2018**, *54*, 8200904. [CrossRef]
22. Du, Y.; Huang, Y.; Guo, B.; Peng, F.; Dong, J. Semianalytical model of multiphase Halbach array axial flux permanent-magnet motor considering magnetic saturation. *IEEE Trans. Transp. Electrif.* **2023**, *9*, 2891–2901. [CrossRef]
23. Wu, J.; Wang, S.; Hu, Y.; Zhang, B.; Xu, X. Modeling and analysis of quasi-3D equivalent magnetic network of direct-drive inner boost permanent magnet motor. *IEEE Access* **2025**, *13*, 304–315. [CrossRef]
24. Forstner, G.; Kugi, A.; Kemmetmüller, W. A magnetic equivalent circuit based modeling framework for electric motors applied to a PMSM with winding short circuit. *IEEE Trans. Power Electron.* **2020**, *35*, 12285–12295. [CrossRef]